Journal of Computational Physics 229 (2010) 813–827

Contents lists available at ScienceDirect

Journal of Computational Physics

journal homepage: www.elsevier.com/locate/jcp

A tangent-plane marker-particle method for the computation of three-dimensional solid surfaces evolving by surface diffusion on a substrate

Ping Du [a], Mikhail Khenner [b,1], Harris Wong [a,*]

[a] Department of Mechanical Engineering, Louisiana State University, Baton Rouge, LA 70803, United States
[b] Department of Mathematics, Western Kentucky University, Bowling Green, KY 42101, United States

ARTICLE INFO

Article history:
Received 14 August 2007
Received in revised form 7 October 2009
Accepted 8 October 2009
Available online 21 October 2009

Keywords:
Surface diffusion
Thin solid films
Contact lines
Surface shape
Nonlinear PDEs
Stability of solutions
Marker-particle methods

ABSTRACT

We introduce a marker-particle method for the computation of three-dimensional solid surface morphologies evolving by surface diffusion. The method does not use gridding of surfaces or numerical differentiation, and applies to surfaces with finite slopes and overhangs. We demonstrate the method by computing the evolution of perturbed cylindrical wires on a substrate. We show that computed growth rates at early times agree with those predicted by the linear stability analysis. Furthermore, when the marker particles are redistributed periodically to maintain even spacing, the method can follow breakup of the wire.

1. Introduction

Capillarity-driven morphological instabilities and evolution of solid micro and nanostructures [29,27,28,5] are important in many branches of materials science and engineering, such as electronic materials processing, crack healing in ceramics, and densification of powder particles during sintering. For a microelectronic or optoelectronic device to function properly, the structural integrity of the thin films must be maintained [18,15,35,36]. This requirement becomes more stringent as the component size of integrated circuits decreases. Thus, characterization of thin film deformation is becoming one of the more important issues in the reliability of integrated circuits.

Several methods have been proposed for direct computation of 3D solid deformation by surface diffusion. The level-set methods were developed by Smereka [33] and Smith et al. [34], the finite-element methods by Burger [3], Bänsch et al. [1], Hausser and Voigt [14], Mayer [21], and Deckelnick et al. [9], and the finite-difference method by Zhang [44]. Most of these methods allow for surface topology changes and for implicit time stepping, and some allow for strong crystalline anisotropy and associated formation of corners and cusps. However, with the exception of Ref. [34], all cited methods are for closed or open periodic surfaces freely suspended in space. The method of Ref. [34] is capable of computing the deforming contact lines, but it requires $N-1$ level set functions if N phases are present, plus complicated and delicate procedure to prevent formation of vacuum or overlaps at junctions of phases. All cited methods employ gridding of either the surface,

* Corresponding author. Tel.: +1 225 578 5893; fax: +1 225 578 5924.
E-mail addresses: mikhail.khenner@wku.edu (M. Khenner), hwong@lsu.edu (H. Wong).
[1] Tel.: +1 270 745 2797; fax: +1 270 745 3699.

0021-9991/$ - see front matter © 2009 Elsevier Inc. All rights reserved.
doi:10.1016/j.jcp.2009.10.013

or of the three-dimensional space (as in the level set method). The level set and the finite-difference methods require numerical differentiation. The finite-element methods usually require complex mesh regularization and triangulation's angle control, at least at large times.

In this paper we describe a meshless particle method for computing evolving solid surfaces which are in contact with a material boundary (substrate) at all times [42,20,19]. In crystal growth such setup is universal, since all methods for thin film growth rely on deposition from the vapor phase or by means of atomic beams. We choose to model a cylindrical solid wire on a substrate as it evolves by surface diffusion. It is assumed that the wire has been pre-grown in such a way that its axis is parallel to the substrate. In the following, we call such wire *supported*, while one that is free of contact with any material boundary is called a *free* wire. The cross-sectional shape of the wire is a part-circle with small perturbations imposed in the axial and circumferential directions. We assume isotropic surface energy in this paper.

The surface and the three-phase contact lines formed among the film, substrate and air are explicitly tracked. We make no assumption as to the smallness of the surface slope and allow any values of a contact angle α in $(0,\pi)$. Surface overhangs are handled naturally in our method. The method uses biquadratic interpolation for the computation of the surface normal and (mean) curvature, and the surface Laplacian of mean curvature. We perform most of the computations in the local tangent-plane coordinate system where the surface Laplacian is greatly simplified (Front-tracking methods employing marker particles have been long in use (and proved very successful) for direct numerical simulations of multiphase fluid flows and solidification. The very extensive list of contributors and bibliography can be found in the review paper by Tryggvason et al. [38]).

The linear stability of supported circular wires with isotropic surface energy was considered by McCallum et al. [22], and with anisotropic surface energy by Gurski et al. [13]. The linear stability of free circular wires with isotropic surface energy, with respect to axial or circumferential perturbations was examined by Nichols and Mullins [30]. Surface energy anisotropy was factored in the linear stability analysis of free wires by Cahn [4] and Gurski and McFadden [12] (In a related study, Kan and Wong [16] considered the three-dimensional linear stability of a two-dimensional profile of a retracting edge of a film on a substrate (assuming isotropic surface energy) [15,8,43] and found one unstable mode of perturbation; thus the edge becomes wavy when perturbed. They determined the growth rate of the perturbation as a function of the wavelength of the perturbation and the speed of the receding edge).

This problem of stability of cylindrical wires can be traced back to Plateau and Lord Rayleigh [31,32]. Rayleigh found that free, inviscid, capillary liquid threads are unstable to small axisymmetric perturbations whose wavelengths are greater than the circumference of the undisturbed thread. Under the action of instability, the thread would tend to decompose in isolated liquid droplets [25]. These conclusions hold also for the solid, free cylindrical wires with isotropic surface energy [30]. For such wires, all purely non-axisymmetric disturbances decay. Rayleigh instability of supported copper, gold and platinum nanowires was experimentally demonstrated [37,17,45]. The kinetic Monte Carlo simulations of instability development due to axisymmetric perturbation (in a free wire) were performed by Muller et al. [26] and gave predictions consistent with the Nichols and Mullins analysis.

This paper aims to present the new method and to validate it by computing the evolution of perturbed surfaces to equilibrium, which could be wires if the perturbation is stable or drops if the perturbation is unstable. Physical implications/discussion will be presented elsewhere. It must be noted that we do not restrict the perturbation to axisymmetric form (Stability and dynamics in the axisymmetric case for free cylindrical wires have been extensively studied using analytical and numerical methods; most notably, see Refs. [7,6,41,2]).

2. Problem formulation

When a solid film evolves by capillarity-driven surface diffusion, the film surface displaces with a normal velocity that obeys [29]

$$V_n^* = B(\nabla_s^* \cdot \nabla_s^*)\kappa^*, \tag{1}$$

where ∇_s^* is the surface gradient operator, $\kappa^* = \nabla^* \cdot \mathbf{n}$ is the surface mean curvature (termed simply "curvature" below), $\mathbf{n}$ is the unit outward normal to the surface, and B is a material constant. Superscript * denotes dimensional variables. This equation is derived using the fact that the chemical potential varies linearly with the curvature of the solid film surface. If the surface curvature is not uniform, then a gradient in chemical potential exists. This gradient drives a surface flux, which redistributes mass along the solid surface. The net effect is that the solid surface moves in the normal direction.

To demonstrate the tangent-plane method, we simulate the evolution of a supported wire with the cross-sectional shape of a part-circle (Fig. 1). The radius of the circle is R_0 which is used as the length scale. Time is made dimensionless by R_0^4/B. In dimensionless variables, Eq. (1) reads

$$\frac{d\mathbf{r}}{dt} \cdot \mathbf{n} = V_n = \nabla_s^2(\nabla \cdot \mathbf{n}), \tag{2}$$

where $\mathbf{r}(t) = x(t)\mathbf{i} + y(t)\mathbf{j} + z(t)\mathbf{k}$ is the position vector of a point on a surface. The Cartesian coordinates (x, y, z) are defined with y pointing in the axial direction and z pointing upward, as shown in Fig. 1. These coordinates form the global coordinate system. The governing, fourth-order Eq. (2) is subject to the following boundary conditions. At the contact line $x = x_c(y)$, the

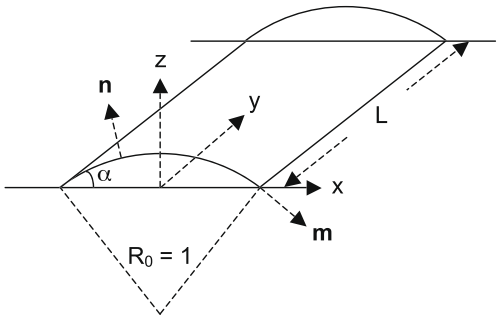

Fig. 1. An unperturbed wire in the shape of part-circle on a substrate. The radius of the circle is R_0, which is used to make the system dimensionless. The length of the computational domain is L. The wire surface has unit normal **n** and contacts the substrate with an equilibrium angle α. The unit vector **m** is tangent to the wire surface and normal to the contact line. A Cartesian coordinate system is defined.

height h of the wire surface is zero, the contact angle is in equilibrium, and the mass flux tangent to the wire surface and into the substrate is zero [16,24,23]:

$$h = 0, \tag{3}$$

$$\mathbf{n} \cdot \mathbf{k} = \cos\alpha, \tag{4}$$

$$\mathbf{m} \cdot \nabla_s \kappa = 0, \tag{5}$$

where $0 < \alpha < \pi$ is the equilibrium contact angle, and **m** is the unit vector tangent to the wire surface and normal to the contact line. The contact line position $x = x_c(y)$ is unknown and must be determined as part of the solution, making this a free-boundary problem. At the two symmetry planes of the wire $y = 0$ and $y = L$, we impose the symmetry condition:

$$\frac{\partial F}{\partial y} = 0, \tag{6}$$

where F represents any quantity that crosses the symmetry boundaries. Eq. (2) and the boundary conditions (3)–(6) are supplemented by an initial condition described below. A cylindrical coordinate system (r, θ, y) is defined with its origin coinciding with the origin of the global Cartesian coordinates (x, y, z) and $\theta = 0$ is aligned with the x-axis (Fig. 1). Thus, the circular arc cross-section of the equilibrium surface is described by

$$r_e(\theta) = \sqrt{1 - \cos^2\alpha\cos^2\theta} - \cos\alpha\sin\theta, \quad 0 \leqslant \theta \leqslant \pi. \tag{7}$$

At $t = 0$, we impose a small periodic perturbation:

$$r = r_e(\theta) + \delta\cos(ky)\cos(p\theta), \tag{8}$$

where δ is the small amplitude ($|\delta| \ll 1$), k is the wavenumber and $p = 0, 1, 2, \ldots$. The perturbation is axisymmetric when $\alpha = \pi/2$ and $p = 0$.

To this end we note that the surface Laplacian operator ∇_s^2 is quite complex [39]:

$$\nabla_s^2 = \frac{1}{a}\left[a_{22}\frac{\partial^2}{\partial x^2} - 2a_{12}\frac{\partial}{\partial x}\frac{\partial}{\partial y} + a_{11}\frac{\partial^2}{\partial y^2} + \kappa a^{1/2}\left(h_x\frac{\partial}{\partial x} + h_y\frac{\partial}{\partial y}\right)\right], \tag{9}$$

where

$$a = 1 + h_x^2 + h_y^2, \quad a_{11} = 1 + h_x^2, \quad a_{22} = 1 + h_y^2, \quad a_{12} = h_x h_y \tag{10}$$

and

$$\kappa = -\frac{a_{22}h_{xx} - 2a_{12}h_{xy} + a_{11}h_{yy}}{a^{3/2}}. \tag{11}$$

As a rule, the numerical evaluation of high-order derivatives in the RHS of Eq. (2) incurs large errors. It is therefore highly desirable to construct the numerical method that uses a simpler form of ∇_s^2 and/or does not call for such numerical differentiation.

3. The marker-particle method

The marker-particle method is implemented in seven steps: (i) place marker particles on a solid surface; (ii) fit a tangent plane to each particle; (iii) locate five closest particles for each particle and transform their global coordinates to the local tangent-plane coordinates; (iv) calculate the surface curvature κ in the local coordinates; (v) evaluate $\nabla_s^2\kappa$ in the local coor-

dinates; (vi) march the particles forward in time; and (vii) update the contact-line particle positions. This finishes one time step.

3.1. Initial marker distribution

We place chosen number of marker particles on the surface described by Eq. (8). For convenience, these particles initially are arranged to be evenly spaced in the axial and azimuthal directions. As the computation proceeds, the surface often becomes greatly deformed, and some neighboring particles may move too close together. This will limit the time step size. Hence, we redistribute the particles periodically to maintain even spacing among them. However, for the purpose of computing the initial growth rate, the redistribution is not needed.

3.2. Tangent-plane construction

A marker particle is described as interior if it is neither on the contact lines nor on the symmetry planes. For a given interior particle P_1 with global coordinates (x_1, y_1, z_1), we find a cluster of five closest marker particles $(x_k, y_k, z_k), k = 2, \ldots, 6$, and fit a sphere of yet unknown radius R through the particle P_1 and three closest particles (i.e., fit to $(x_k, y_k, z_k), k = 1, \ldots, 4$). This determines the sphere center (x_0, y_0, z_0) (which is generally not on the surface), and R. The cost of this construction is the solution of a 3×3 linear algebraic system. The sphere center together with particle P_1 yields the surface unit normal vector at P_1:

$$\mathbf{n} = l_z\mathbf{i} + m_z\mathbf{j} + n_z\mathbf{k} \equiv \frac{x_1 - x_0}{R}\mathbf{i} + \frac{y_1 - y_0}{R}\mathbf{j} + \frac{z_1 - z_0}{R}\mathbf{k}. \tag{12}$$

We define two orthogonal unit vectors in the tangent plane as

$$\mathbf{e}_x = l_x\mathbf{i} + m_x\mathbf{j} + n_x\mathbf{k}, \quad \mathbf{e}_y = l_y\mathbf{i} + m_y\mathbf{j} + n_y\mathbf{k}, \tag{13}$$

and make them obey $\mathbf{e}_x = \mathbf{n} \times \mathbf{j}$ and $\mathbf{e}_y = \mathbf{n} \times \mathbf{e}_x$. Thus,

$$l_x = -\frac{n_z}{\sqrt{n_z^2 + l_z^2}}, \quad m_x = 0, \quad n_x = \frac{l_z}{\sqrt{n_z^2 + l_z^2}}, \tag{14}$$

$$l_y = m_z n_x, \quad m_y = l_x n_z - l_z n_x, \quad n_y = -l_x m_z. \tag{15}$$

This tangent plane at P_1 may not be truly tangent to the surface owing to the spherical fit. However, we show later that this error in finding the normal vector at P_1 is eliminated by using the full expressions for curvature and surface Laplacian.

3.3. Transformation to local tangent-plane coordinates

Global coordinates of the five particles P_2–P_6 closest to particle P_1 are transformed to local tangent-plane coordinates (X, Y, Z) as follows:

$$\begin{aligned} X_k &= l_x(x_k - x_1) + m_x(y_k - y_1) + n_x(z_k - z_1), \\ Y_k &= l_y(x_k - x_1) + m_y(y_k - y_1) + n_y(z_k - z_1), \\ Z_k &= l_z(x_k - x_1) + m_z(y_k - y_1) + n_z(z_k - z_1) \quad , k = 2, \ldots, 6. \end{aligned} \tag{16}$$

The tangent-plane coordinate system (X, Y, Z) has origin at $P_1(0, 0, 0)$ and the axis Z is along the surface normal $\mathbf{n}$.

3.4. Computation of curvature κ

First, we fit the cluster particles by a biquadratic polynomial $H(X, Y)$:

$$H = a_1X^2 + a_2XY + a_3Y^2 + a_4X + a_5Y + a_6. \tag{17}$$

Since $P_1(0, 0, 0)$ is one of the particles, $a_6 = 0$. The cost of determining the coefficients $a_i, i = 1, \ldots, 5$, is the solution of a 5×5 linear algebraic system:

$$Z_k = a_1X_k^2 + a_2X_kY_k + a_3Y_k^2 + a_4X_k + a_5Y_k \quad , k = 2, \ldots, 6. \tag{18}$$

The coefficients a_4 and a_5 must be zero whenever the tangent plane is exact, because in this case $H_X = H_Y = 0$ at $(X, Y) = (0, 0)$. However, since a spherical fit is used in finding the normal vector at P_1, leading to the tangent plane not exactly tangent to the surface at P_1, the coefficients a_4 and a_5 are non-zero. Their values are usually very small (~ 0.01).

We can now compute the curvature at P_1 using Eq. (11):

$$\kappa^{(1)} = -\frac{2(1 + a_5^2)a_1 - 2a_4a_5a_2 + 2(1 + a_4^2)a_3}{(1 + a_4^2 + a_5^2)^{3/2}}. \tag{19}$$

Since the curvature is calculated using the full expression, the error in finding the normal vector at P_1 has no effect on $\kappa^{(1)}$. The only discretization error comes from approximating the surface around P_1 by the biquadratic polynomial in Eq. (17). Also note that in the time stepping procedure we use corrected normal vectors, which are calculated from Eq. (17) (see Section 3.6).

The local coordinate set $\{X_k, Y_k, Z_k\}, k = 1, \ldots, 6$ is memorized for each interior marker particle since it is required in Section 3.5. Before the surface Laplacian could be computed at each interior particle, we need to find surface curvatures at the contact lines and symmetry planes.

3.4.1. Computation of surface curvature at the contact lines

This curvature can be computed by imposing the zero mass-flux condition in Eq. (5) either with a first or second-order accuracy numerical method. The first-order-accurate method sets the curvature at each contact-line marker equal to the curvature at the closest interior marker location. To implement the second-order accurate method, we find two closest interior particles, compute distances from the contact-line marker particle to these particles and, using the distance as an independent variable, compute the one-sided first derivative of the curvature function. After setting this derivative to zero we obtain the desired curvature. One-sided differentiation on non-uniform three-point grids is done using the subroutine WEIGHTS [11]. Our numerical experiments with the two methods show no significant gain in the overall accuracy for the second-order method. The results presented in Section 4 are obtained with the first-order method.

3.4.2. Computation of surface curvature at the symmetry boundaries

The surface curvatures at the symmetry planes $y = 0$ and $y = L$ are calculated by imposing the symmetry condition (6). The unit normal vector $\mathbf{n}$ at each particle on the symmetry plane must lie in the plane, i.e., $m_z = 0$ in Eq. (12). Thus, $\mathbf{n}$ at particle P_1 is calculated by fitting a circular arc through P_1 and two closest adjacent particles P_2 and P_3 on the plane. Once $\mathbf{n}$ is found, a tangent plane can be constructed at P_1 following Eqs. (13)–(15), and local tangent-plane coordinates (X, Y, Z) can be defined following Eq. (16). In the local coordinates, the symmetry plane is located at $Y = 0$, and the symmetry condition (6) becomes $\partial/\partial Y = 0$ at $Y = 0$. If the biquadratic polynomial $H(X, Y)$ in Eq. (17) is fitted to the surface at P_1, then the symmetry condition demands $\partial H/\partial Y = 0$ at $Y = 0$, yielding $a_2 = a_5 = 0$. Hence, the biquadratic polynomial reduces to $H = a_1X^2 + a_3Y^2 + a_4X$. To find the coefficients, an interior particle P_4 closest to P_1 is located, and together with P_2 and P_3 is sufficient to determine the coefficients. The surface curvature κ at P_1 is then found from Eq. (19).

3.5. Computation of $\nabla_s^2\kappa$

For each interior particle P_1, we fit curvature κ for the five closest particles P_2–P_6 by a biquadratic polynomial $\kappa(X, Y)$, i.e.,

$$\kappa = b_1X^2 + b_2XY + b_3Y^2 + b_4X + b_5Y + b_6, \tag{20}$$

where $b_6 = \kappa(0, 0) = \kappa^{(1)}$ is the curvature at P_1 and is known. The cost of determining the coefficients $b_i, i = 1, \ldots, 5$ is the solution of a 5×5 linear algebraic system. The full Laplacian operator in Eq. (9) translates into

$$\left(\nabla_s^2\kappa\right)^{(1)} = 2\frac{(1 + a_5^2)b_1 - a_4a_5b_2 + (1 + a_4^2)b_3}{1 + a_4^2 + a_5^2} + \frac{b_6(a_4b_4 + a_5b_5)}{(1 + a_4^2 + a_5^2)^{1/2}}. \tag{21}$$

Since the surface Laplacian is computed at $P_1(0, 0, 0)$, b_4 and b_5 are all that remains of the otherwise more complicated expressions for $\partial\kappa/\partial x$ and $\partial\kappa/\partial y$ in the last term of Eq. (9). Furthermore, the full surface Laplacian also implies that the error in finding the surface normal at P_1 has no effect on the accuracy of $\nabla_s^2\kappa$. Computation of $\nabla_s^2\kappa$ is repeated for all interior marker particles.

3.5.1. Computation of $\nabla_s^2\kappa$ at the contact lines

There is no need to calculate $\nabla_s^2\kappa$ for the marker particles at the contact lines because the particles are advanced in time by imposing the boundary conditions (3)–(5), and not by the evolution Eq. (2), as described in Section 3.7.

3.5.2. Computation of $\nabla_s^2\kappa$ at the symmetry boundaries

The computation of $\nabla_s^2\kappa$ is similar to the procedure of calculating surface curvatures. When the symmetry condition (6) is applied to Eq. (20), we get $\partial\kappa/\partial Y = 0$ at $Y = 0$. This gives $b_2 = b_5 = 0$. Thus, we can solve the remaining three coefficients in Eq. (20) using curvatures at P_2, P_3, and P_4, the particles used in the curvature calculation. Once Eq. (20) is known, $\nabla_s^2\kappa$ at P_1 follows from Eq. (21).

3.6. Time stepping

Interior particles and particles at symmetry planes are marched forward in time using Euler's method:

$$\mathbf{r}(t + \Delta t) = \mathbf{r}(t) + \mathbf{n}_g V_n \Delta t, \tag{22}$$

where $\mathbf{r} = x\mathbf{i} + y\mathbf{j} + z\mathbf{k}$ is the global position vector of a particle $(P_1), V_n = \nabla_s^2\kappa$, and $\mathbf{n}_g$ is the improved unit normal at P_1 in the global coordinates. To find $\mathbf{n}_g$, we first compute the improved unit normal $\mathbf{N}$ in the local coordinates from the biquadratic polynomial in Eq. (17) as

$$\mathbf{N} = \frac{-a_4\mathbf{I} - a_5\mathbf{J} + \mathbf{K}}{\sqrt{1 + a_4^2 + a_5^2}}, \tag{23}$$

where $\mathbf{I}$, $\mathbf{J}$, and $\mathbf{K}$ are the base vectors of the local coordinate system. In the global coordinate system, $\mathbf{I}$, $\mathbf{J}$, and $\mathbf{K}$ are represented by $\mathbf{e}_x, \mathbf{e}_y$, and $\mathbf{n}$, respectively, as shown in Eqs. (12)–(15). Thus, $\mathbf{N}$ is transformed to $\mathbf{n}_g$ by solving the following three equations:

$$\mathbf{n}_g \cdot \mathbf{e}_x = \mathbf{N} \cdot \mathbf{I}, \quad \mathbf{n}_g \cdot \mathbf{e}_y = \mathbf{N} \cdot \mathbf{J}, \quad \mathbf{n}_g \cdot \mathbf{n} = \mathbf{N} \cdot \mathbf{K}. \tag{24}$$

These three equations determine the three components of $\mathbf{n}_g$. The improved unit normal $\mathbf{n}_g$ eliminates the error in the normal vector in Eq. (12).

To ensure numerical stability and to enhance marching speed, the time step Δt varies as

$$\Delta t = C_t(\Delta s)^4, \tag{25}$$

where Δs is the minimum distance between any two particles at time t and C_t is a constant determined by trial-and-error. The value of C_t stays fixed for each computation and varies from 0.0258 to 0.0487 for different wires.

3.7. Propagation of contact lines

After the interior particles have been marched forward one time step, the contact-line particle positions are updated by imposing the boundary conditions (3)–(5). For each contact-line particle P_1, we find the closest marched interior particle $P_2(x_2, y_2, z_2)$ with improved normal vector $\mathbf{n}_g(l_z, m_z, n_z)$. This normal vector is never vertical because P_2 is close to the contact line and the contact angle $\alpha \neq 0$ or π. Hence, $\mathbf{n}_g$ is inclined in a direction that is perpendicular to the contact line. We define a vertical plane that contains point P_2 and $\mathbf{n}_g$, so that the plane is perpendicular to the contact line. In this vertical plane, we fit a circular arc that passes through P_2 with the center along $\mathbf{n}_g$ and contacts the substrate with angle α. The contact point is the new $P_1(x_1, y_1, 0)$ where

$$\begin{aligned} x_1 &= x_2 + \frac{z_2 l_z}{\cos\alpha - n_z}\left(1 - \frac{\sin\alpha}{\sqrt{l_z^2 + m_z^2}}\right), \\ y_1 &= y_2 + \frac{z_2 m_z}{\cos\alpha - n_z}\left(1 - \frac{\sin\alpha}{\sqrt{l_z^2 + m_z^2}}\right). \end{aligned} \tag{26}$$

The circular-arc fit gives $\nabla_s\kappa = 0$ along the arc. In this way, both the zero mass-flux and the contact angle conditions are satisfied. For the contact-line particles at the symmetry planes, we constrain P_2 to lie at the symmetry plane, leading to a new P_1 always at the symmetry plane. Thus, all contact-line positions are updated (see Du [10] for details). This method is valid for $0 < \alpha < \pi$.

4. Validation

4.1. Volume

Surface diffusion does not alter the mass or volume of the wire. Thus, the wire volume is a good indicator of the accuracy of our numerical method. The volume V of the wire can be expressed as

$$V = \frac{1}{3}\int\int\int_V (\nabla \cdot \mathbf{x})dV = \frac{1}{3}\oint\!\!\oint_A (\mathbf{x} \cdot \mathbf{n})dA, \tag{27}$$

where $\mathbf{x} = x\mathbf{i} + y\mathbf{j} + z\mathbf{k}$ is the three-dimensional position vector of a point in the wire, $\mathbf{n} = n_x\mathbf{i} + n_y\mathbf{j} + n_z\mathbf{k}$ is the unit normal vector of the surface pointing outward from the wire, and A is the wire surface that includes two end surfaces at symmetry planes, the cylindrical surface, and the substrate surface. Thus, $V = V_{y=0} + V_{y=L} + V_s + V_c$, where the subscript s and c represent the substrate and the cylindrical surface, respectively. We calculate the volume of the wire by evaluating the surface integral on four surfaces separately.

On the substrate surface, the contact-line particles have coordinate $z = 0$ and surface normal vector $\mathbf{n} = -\mathbf{k}$. Thus, we get $\mathbf{x} \cdot \mathbf{n} = 0$, and $V_s = 0$.

Similarly, on the symmetry surface $y = 0$, we have $V_{y=0} = 0$ because $\mathbf{n} = -\mathbf{j}$ and $\mathbf{x} \cdot \mathbf{n} = 0$.

On the symmetry surface at $y = L, \mathbf{x}\cdot\mathbf{n} = L$ since $\mathbf{n} = \mathbf{j}$ and $\mathbf{x} = x\mathbf{i} + L\mathbf{j} + z\mathbf{k}$. Thus, $V_{y=L} = LA_{y=L}/3$. According to Green's theorem, $A_{y=L} = 1/2\int\int_A(\nabla\cdot\mathbf{x})dA = 1/2\oint(xdz - zdx)$. Using the rectangular approximation, we get

$$V_{y=L} = \frac{L}{6}\sum_{i=1}^{N_e-1}(x_i z_{i+1} - z_i x_{i+1}), \tag{28}$$

where N_e is the number of particles on the symmetry surface.

The last surface is the cylindrical surface. This surface is approximated by triangular surfaces formed by connecting all adjacent marker particles. The area of the ith triangle formed by three particles at $\mathbf{x}_{i1}, \mathbf{x}_{i2}$, and $\mathbf{x}_{i3}$ is $A_i = \frac{1}{2}|(\mathbf{x}_{i1} - \mathbf{x}_{i2}) \times (\mathbf{x}_{i2} - \mathbf{x}_{i3})|$. We also take $(\mathbf{x}\cdot\mathbf{n})_i = (\mathbf{x}_{i1}\cdot\mathbf{n}_{i1} + \mathbf{x}_{i2}\cdot\mathbf{n}_{i2} + \mathbf{x}_{i3}\cdot\mathbf{n}_{i3})/3$, where $\mathbf{n}_{ij}$ is the improved unit normal vector at $\mathbf{x}_{ij}$, $j = 1, 2, 3$. The volume on this surface can be expressed as

$$V_c = \frac{1}{3}\sum_{i=1}^{M}(\mathbf{x}\cdot\mathbf{n})_i A_i, \tag{29}$$

where M is the total number of triangles on the cylindrical surface. The variables used in Eqs. (28) and (29) are readily available from the numerical solution. Thus, the volume of the wire $V = V_{y=L} + V_c$ can be calculated without additional interpolation.

We calculate the volume of initially unperturbed wires with different particle numbers and find that the method is second-order accurate. We also compute the volume as a function of time. For all decaying cases, the volume varies at most by about 1%.

4.2. Surface normal velocity versus time

We compute the evolution of wires with three different contact angles $\alpha = \pi/2, \pi/4$, and $3\pi/4$. For each wire, the equilibrium surface profile in Eq. (7) is perturbed according to Eq. (8) with $\delta = 0.01, p = 0$ or 2, and $k = \pi/L$, where L is the axial length of the computational domain. The perturbation in Eq. (8) has wavelength 2L in the axial direction. However, owing to symmetry, we only need to follow wire evolution in $0 \leqslant y \leqslant L$. Since the initial perturbation in Eq. (8) is not an eigenmode, it can be decomposed into several eigenmodes that decay or grow exponentially at different rates. For a stable perturbation, the fundamental mode decays the slowest, and is the one observed at the end. Thus, after some time, our computed decay rate should approach that of the fundamental mode derived by the linear stability analysis. In the unstable case, the normal velocity grows exponentially with time initially. The growth rate can also be compared with that predicted by the linear stability theory.

To compare with linear stability predictions, we extrapolate computed growth rates to zero particle spacing. For each perturbed wire, we analyze the surface normal velocity as a function of time for two marker particles located at the interceptions between the mid-plane $x = 0$ and the symmetry planes $y = 0$ and $y = L$. These two particles always stay at the same (x, y) positions as we vary the particle number N. Hence, their normal velocities can be compared for different N. For each wire, we select four different N such that the initial spacing has the ratio 1, 1/2, 1/4, and 1/8 among the cases. The computed normal velocity at each grid-invariant particle is fitted by an exponential function to yield the growth rate. The fitting is carried out over a range of time that shows the best regression value for all four N cases. For each N, the two growth rates at the two grid-invariant particles are averaged. The average growth rate is then plotted as a function of initial particle spacing ($\sim 1/N$) and fitted by a quadratic curve. The curve is extrapolated to zero particle spacing to give a growth rate that is independent of particle spacing. This growth rate is compared with the linear stability prediction. By varying the time step and N, we find that our numerical method is first-order accurate in time and second-order accurate in space, as expected.

4.3. $\alpha = \pi/2$

For $\alpha = \pi/2$, the supported wire behaves as a free wire. An analytic solution can be derived for the growth rate σ by the linear stability analysis (Appendix A):

$$\sigma = \left(p^2 + k^2\right)\left(1 - p^2 - k^2\right). \tag{30}$$

We first consider a perturbed wire with $L = 1, k = \pi$ and $p = 0$. According to Eq. (30), the perturbation is stable with growth rate $\sigma = -87.54$. We use four particle numbers $N = 44, 147, 533$, and 2025, and time step Δt that follows Eq. (25). In Fig. 2, we plot the normal surface velocity V_n versus time computed using $N = 2025$ for the two grid-invariant marker particles at $y = 0$ and $y = L$. The growth rates are found by an exponential fit to be -87.26 and -87.28. The exponential fits are also plotted in Fig. 2 and are indistinguishable from each other. The average value $\sigma = -87.27$ together with other N cases is plotted in Fig. 3 as a function of Δs_0, which is the minimum particle spacing at $t = 0$. A quadratic fit to the data yields $\sigma = -87.68 + 4.009\Delta s_0 + 153.2\Delta s_0^2$. Thus, at $\Delta s_0 = 0$, we get $\sigma = -87.68$, which compares well with the linear stability result.

We then change p from 0 to 2 to study the effect of azimuthal perturbation. We follow the procedure described above, and find that the extrapolated growth rate at zero particle spacing is $\sigma = -178.6$, which is close to the predicted value $\sigma = -178.5$ using Eq. (30).

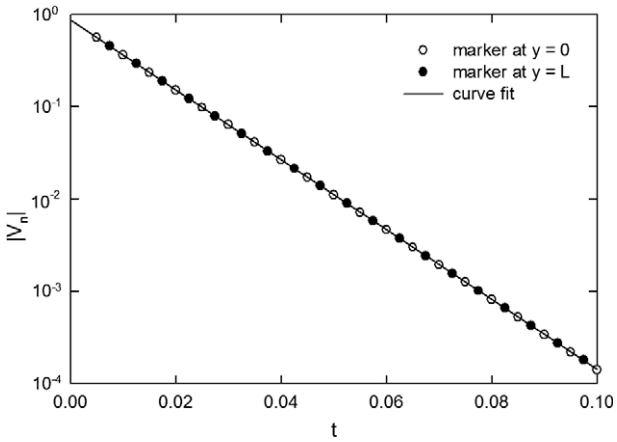

Fig. 2. Normal surface velocity V_n versus time for the two grid-invariant marker particles at $y = 0$ and $y = L$. The computation is performed using $\alpha = \pi/2, L = 1, \delta = 0.01, k = \pi, p = 0$, and $N = 2025$. The results are fitted by an exponential function in the range $t = 0.02 - 0.06$, which shows the highest regression value.

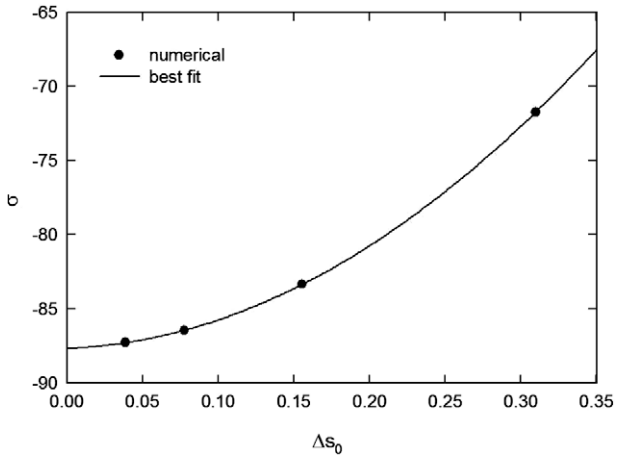

Fig. 3. Growth rate σ versus initial minimum grid spacing Δs_0 for $\alpha = \pi/2, L = 1, \delta = 0.01, k = \pi$, and $p = 0$. A quadratic best fit is also plotted.

We also study an unstable case with $L = 4, k = \pi/4, p = 0$, and $N = 2793$. The surface normal velocities increase exponentially with time, as shown in Fig. 4. We fit the data by an exponential function over a range of time that yields the best regression value. The fit gives $\sigma = 0.2377$ and $\sigma = 0.2374$ for the particle at $y = 0$ and $y = L$, respectively. The average value together with those similarly calculated using $N = 56$, 195, and 725 is fitted by a quadratic curve. The curve is extrapolated to zero particle spacing giving $\sigma = 0.2368$. The predicted growth rate using Eq. (30) is $\sigma = 0.2363$. The wire evolves towards pinch off as shown in Fig. 5, in agreement with axisymmetric calculations [7,6,41,2].

4.4. $\alpha = \pi/4$

We consider $L = \pi, k = 1$, and $p = 0$ or 2. The surface normal velocity V_n computed using $N = 1881$ is plotted in Fig. 6 as a function of time for $p = 0$ (a) and $p = 2$ (b). Fig. 6(a) shows that the perturbation with $p = 0$ is unstable and it grows exponentially in time after some high-order modes have decayed. Fig. 6(b) shows that the $p = 2$ mode is stable and it decays quickly before the $p = 0$ mode starts to grow. The growth rates for $p = 0$ and $p = 2$ are calculated following the procedures described above. We find $\sigma = 1.762$ for $p = 0$ and $\sigma = -222.2$ for $p = 2$. The linear stability analysis gives the corresponding values $\sigma = 1.722$ and -223.9 [40]. The wire profiles at different times for the unstable case $p = 0$ are plotted in Fig. 7.

4.5. $\alpha = 3\pi/4$

We consider a perturbed wire with $L = \pi, k = 1, p = 0$, and $N = 28$, 91, 325, and 1225. We find that the perturbation is stable with extrapolated growth rate $\sigma = -0.2353$, which is close to the linear stability value of $\sigma = -0.2345$ [40].

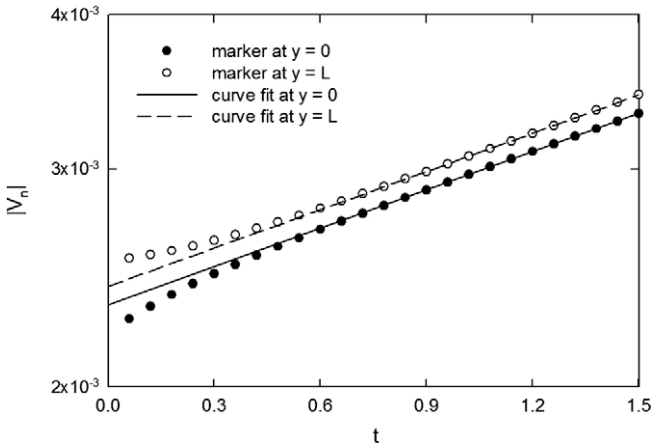

Fig. 4. Normal surface velocity V_n versus time for the two grid-invariant marker particles at $y = 0$ and $y = L$. The computation is performed using $\alpha = \pi/2, L = 4, \delta = 0.01, k = \pi/4, p = 0$, and $N = 2793$. The results are fitted by an exponential function in the range $t = 0.9 - 1.2$, which shows the highest regression value.

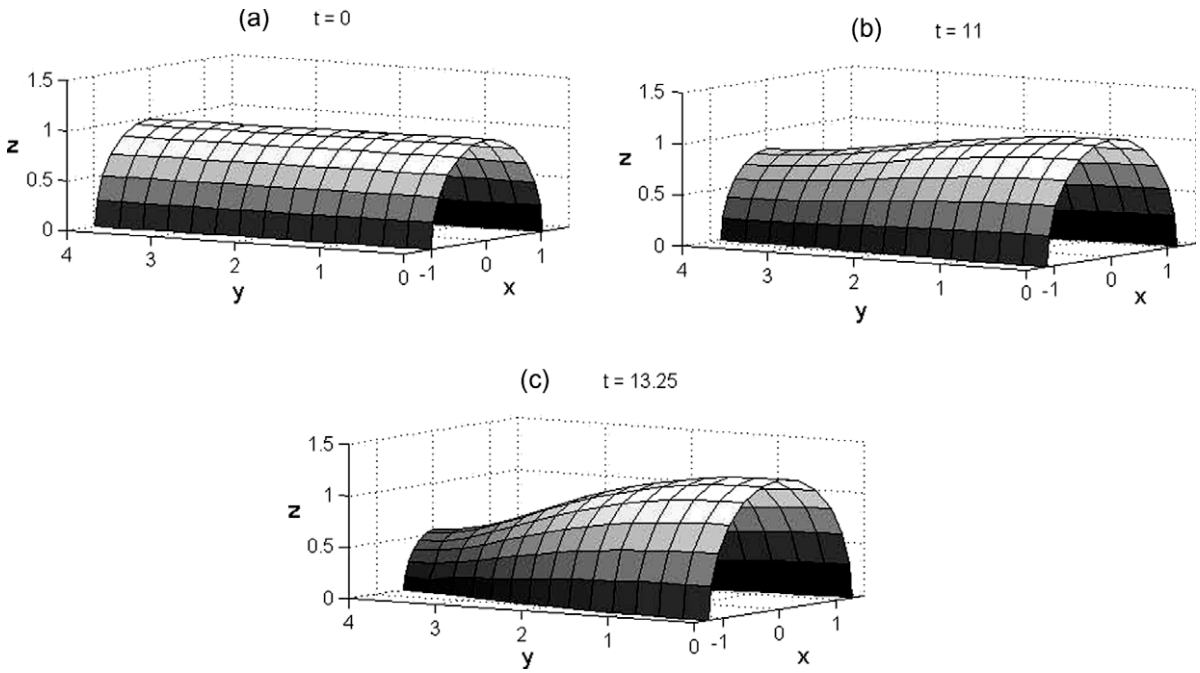

Fig. 5. Wire profiles at time $t = 0$ (a), $t = 11$ (b), and $t = 13.25$ (c) for $\alpha = \pi/2, L = 4, \delta = 0.01$, $k = \pi/4$, and $p = 0$.

We then change L from π to 2π (and k from 1 to 1/2) to study the evolution of a longer wire. For this longer wire, more marker particles are needed and $N = 49$, 169, 625, and 2401. We find that the perturbation is unstable with extrapolated growth rate $\sigma = 0.1371$. This compares well with predicted value $\sigma = 0.1370$ [40]. The wire profiles at different times are shown in Fig. 8.

5. Redistribution of marker particles

As shown in Figs. 5, 7 and 8, the particles move closer at the thin end. Thus, the minimum distance Δs between any two particles decreases with time, and so is the time step Δt, according to Eq. (25). This can make the time marching excruciatingly slow. To alleviate this problem, we redistribute the particles once every 100 time steps to maintain more even sepa-

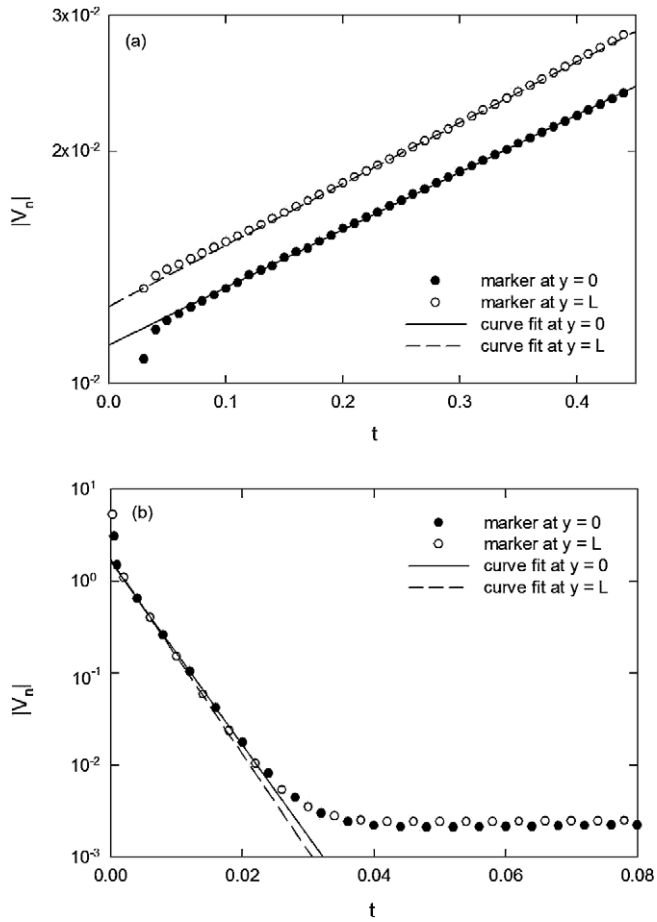

Fig. 6. Normal surface velocity V_n versus time for the two grid-invariant marker particles at $y = 0$ and $y = L$. The computation is performed using $\alpha = \pi/4, L = \pi, \delta = 0.01, k = 1, N = 1881$, and (a) $p = 0$ and (b) $p = 2$. In (a) the results are fitted by an exponential function in the range $t = 0.267 - 0.3$, and in (b) the range is $t = 0.005 - 0.011$. These ranges show the highest regression values.

ration among them. Since the particles redistribute, a nominal particle separation has to be defined and maintained throughout the evolution of the wire. We take the nominal particle separation Δs_0 as the minimum distance between any two particles at time $t = 0$. If two particles are closer than $\Delta s_m = 0.6\ \Delta s_0$, then one of the particles will be eliminated. This elimination is necessary because the total surface area of the wire decreases with time, which is expected for capillarity-driven surface deformation. The particle elimination also allows breakup of the wire. The distribution of particles is carried out in four steps.

5.1. Addition of contact-line particles

When the wire breaks up, it is necessary to add contact-line particles because new contact lines will be created. This is done before the redistribution of interior particles. First, all interior particles that are used in Section 3.7 to march the contact-line particles are identified. Their vertical distances from the substrate are recorded and the maximum height is denoted by h_m. Then, all other interior particles with height $h < h_m$ are assumed to be close to the contact line and each is given a new contact-line particle following Eq. (26). Since new contact lines are created during breakup of wires, this addition of contact-line particles is necessary if we want to follow the breakup process.

5.2. Elimination of interior particles

For each interior particle P_1, we calculate the distance between P_1 and its closest neighbor particle P_2. If the distance $P_1P_2 < \Delta s_m = 0.6\ \Delta s_0$, then P_1 is eliminated. This maintains the minimum separation between any two particles to be greater than Δs_m.

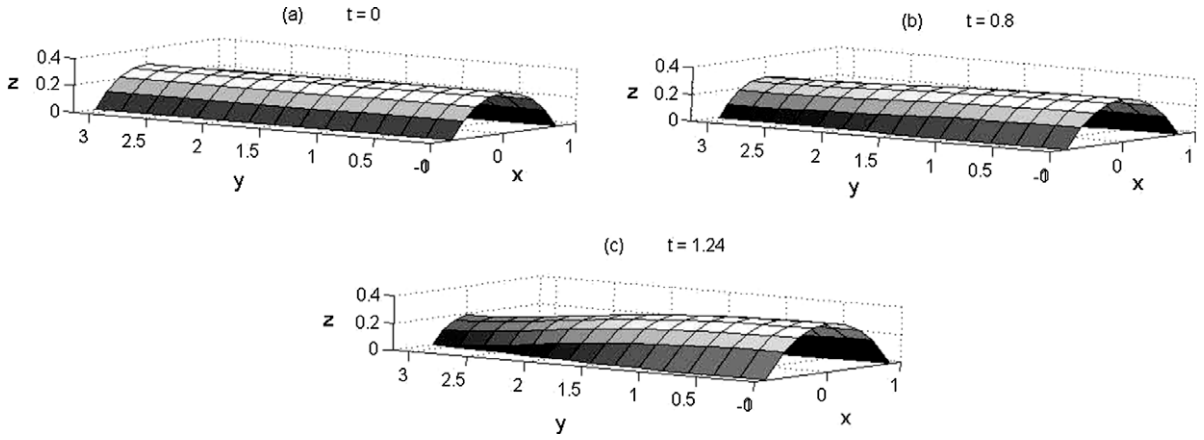

Fig. 7. Wire profiles at time $t = 0$ (a), $t = 0.8$ (b), and $t = 1.24$ (c) for $\alpha = \pi/4, L = \pi, \delta = 0.01, k = 1$, and $p = 0$.

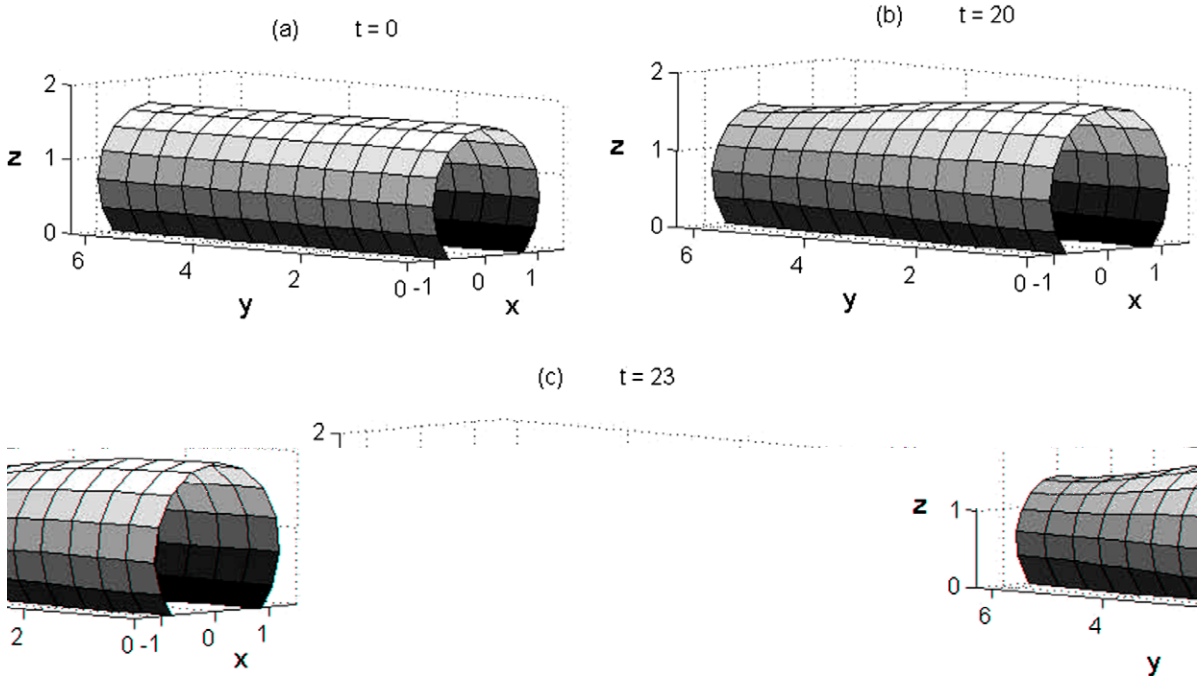

Fig. 8. Wire profiles at time $t = 0$ (a), $t = 20$ (b), and $t = 23$ (c) for $\alpha = 3\pi/4, L = 2\pi, \delta = 0.01, k = 1/2$, and $p = 0$.

5.3. Redistribution of interior particles

For each interior particle P_1, we identify eight closest particles $P_2, \ldots, P_9$, in the ascending order of separation distance. These particles are projected normally onto the local tangent plane of P_1. The projected image of $P_i, i = 2, \ldots, 9$, is assumed to interact with P_1 by a repulsive force:

$$\mathbf{f}_i = -\frac{\mathbf{x}_i - \mathbf{x}_1}{r}\left(\frac{\Delta s_0}{r}\right)^7 \tag{31}$$

where $\mathbf{f}_i$ is the in-plane force acting on P_1 by $P_i, \mathbf{x}_i$ is the position of the projected image of $P_i, \mathbf{x}_1$ is the position P_1, and $r = \mid \mathbf{x}_i - \mathbf{x}_1 \mid$. The total force from the projected images of particle P_2–P_9 on P_1 is calculated, and P_1 is moved by a distance proportional to the total force in the direction of the total force. After this in-plane displacement, P_1 moves to a position on the tangent plane that is more equally separated from P_2 to P_9. This new in-plane position of P_1 is the projected image of P_1,

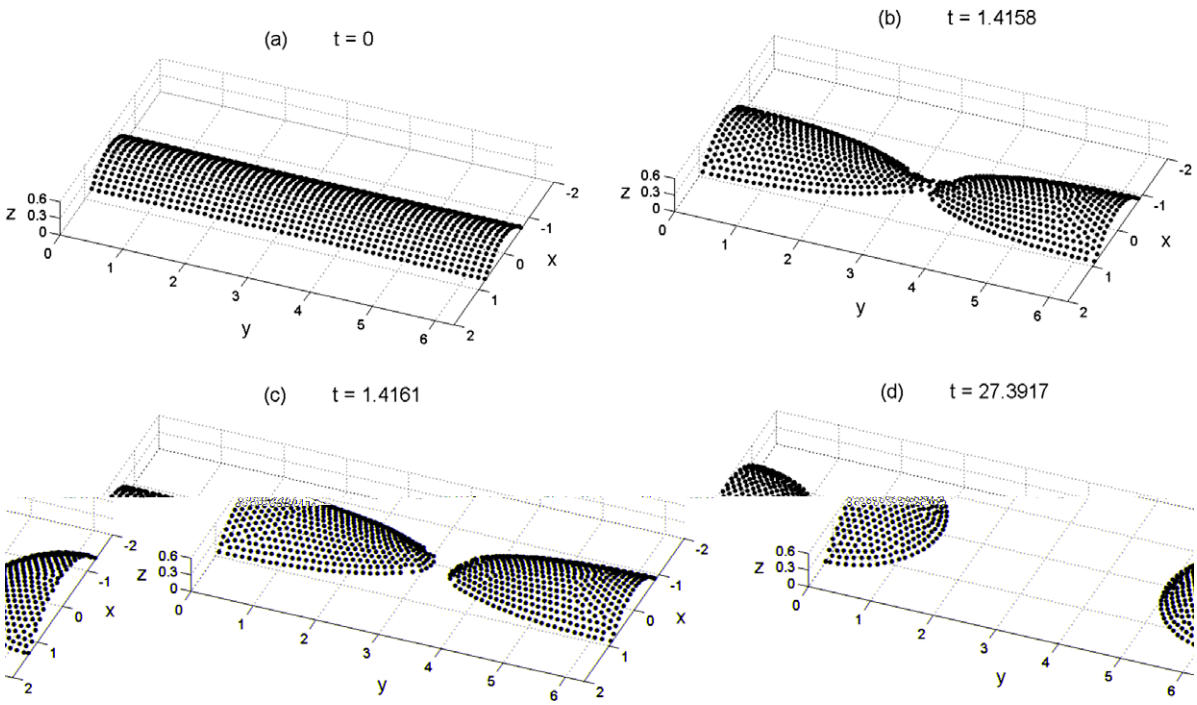

Fig. 9. Wire profiles at four different times for $\alpha = \pi/4, L = \pi, \delta = 0.01, k = 1$, and $p = 0$. The marker particles are plotted as points.

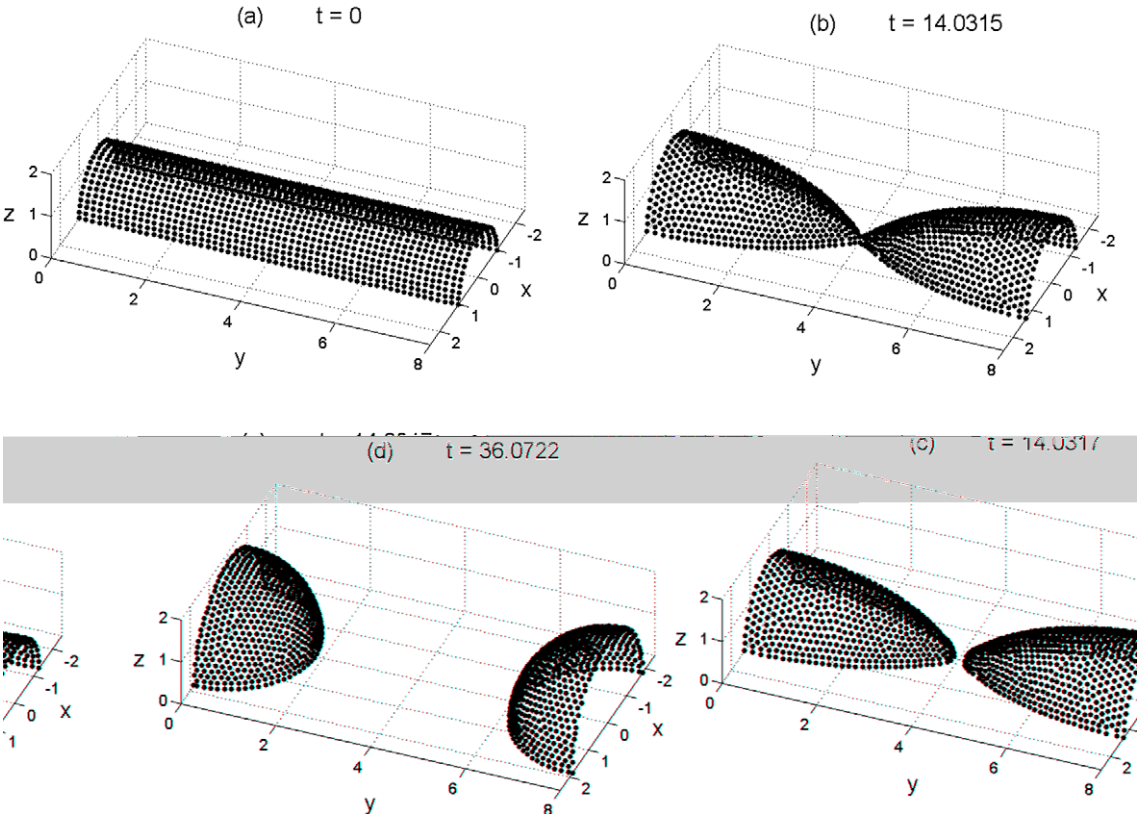

Fig. 10. Wire profiles at four different times for $\alpha = \pi/2, L = 4, \delta = 0.01, k = \pi/4$, and $p = 0$. The marker particles are plotted as points.

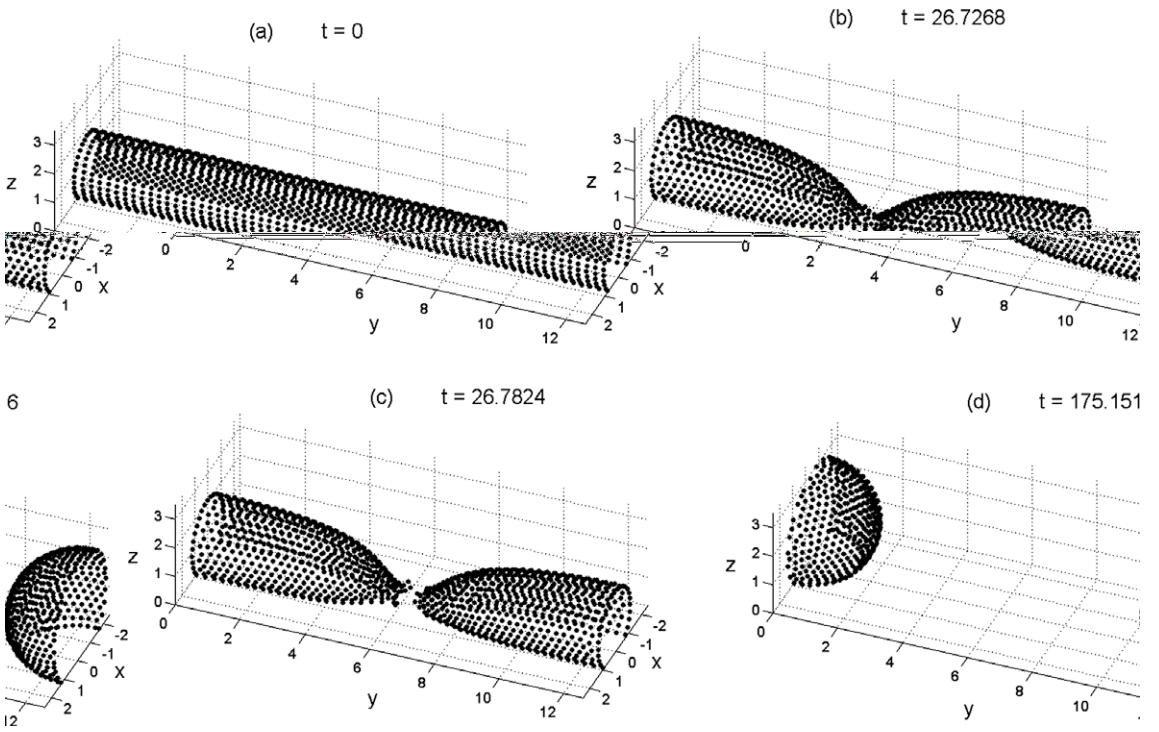

Fig. 11. Wire profiles at four different times for $\alpha = 3\pi/4, L = 2\pi, \delta = 0.01, k = 1/2$, and $p = 0$. The marker particles are plotted as points.

and the normal height of P_1 from the tangent plane is calculated using the biquadratic polynomial in (17). The redistribution is carried out for all interior particles.

At the symmetry planes, a particle P_1 is eliminated if $P_1P_2 < \Delta s_m$, where P_2 is the closest particle on the symmetry plane. Otherwise, P_1 is relocated to the midpoint between P_2 and P_3, where P_3 is the closest particle to P_1 on the symmetry plane on the opposite side from P_2.

5.4. Elimination of contact-line particles

The contact line particles are eliminated as follows. After elimination and redistribution of interior particles, it is possible that two contact-line particles share the same closest interior particle. In that case, one of the two will be eliminated. Thus, only one contact-line particle is associated with one closest interior particle, and the marching scheme in Section 3.7 can be implemented.

Figs. 9–11 show the breakup of wires for different contact angles. To capture breakup, we have to simulate the whole wavelength 2L of an unstable perturbation. No special criterion is imposed to induce breakup. As the neck thins, the particles are concentrated and subsequently dropped if their separation distances are less than Δs_m. Thus, as the neck radius reaches the same order as Δs_m, all the particles at the neck are eliminated, and the wire breaks as a result. Hence, the breakup follows naturally from the particle elimination scheme and no additional criterion is imposed or needed.

6. Conclusions

In this paper the tangent-plane marker-particle method for the computation of 3D morphological evolution of solid surfaces is developed and tested. We demonstrated quadratic convergence in space and matching of surface growth rates to linear theories. The wire volume is conserved during the simulations. The base complexity (per time step) of the method is only

$$C = 2N(C_1 + C_2) + 2N_s(C_3 + C_1) + C_4(N + N_s + N_c) \tag{32}$$

where N is the number of interior marker particles, N_s is the number of symmetry plane particles (excluding the contact line particle on symmetry planes), N_c is the number of contact-line particles, C_1 is the complexity of solving 3×3 linear algebraic system (LAS), C_2 is the complexity of solving 5×5 LAS, C_3 is the complexity of solving 2×2 LAS, and C_4 is the complexity of sorting at most eight real numbers in ascending order.

Acknowledgments

H.W. acknowledges support from National Science Foundation (CMS-0407785).

Appendix A. Linear stability for $\alpha = \pi/2$

Nichols and Mullins [30] studied the linear stability of a free circular wire, but they separated axial and non-axisymmetric perturbations. Here we consider both perturbations simultaneously and derive the growth rate in Eq. (30). It is shown by McCallum et al. [22] that the supported wire having contact angle $\pi/2$ is equivalent, as far as isotropic evolution of morphology is concerned, to a free wire.

Consider the circular wire shown in Fig. 1 and assume $\alpha = \pi/2$. The origin of the cylindrical coordinates (r, θ, y) used in Eq. (7) now is at the center of the wire. If a small perturbation ε is applied, then the wire surface location becomes

$$r(t, \theta, y) = 1 + \varepsilon(t, \theta, y). \tag{A1}$$

When this is substituted into Eq. (2), we get [22]

$$\frac{\partial \varepsilon}{\partial t} = -\left(\frac{\partial^4 \varepsilon}{\partial y^4} + 2\frac{\partial^4 \varepsilon}{\partial^2 y \partial^2 \theta} + \frac{\partial^4 \varepsilon}{\partial \theta^4} + \frac{\partial^2 \varepsilon}{\partial y^2} + \frac{\partial^2 \varepsilon}{\partial \theta^2}\right). \tag{A2}$$

We take

$$\varepsilon = e^{\sigma t} \cos ky \cos p\theta. \tag{A3}$$

This gives Eq. (30). Hence, if $p = 0$ (axisymmetric mode), then $\sigma > 0$ for $k < 1$. If $p \geqslant 1$, then $\sigma \leqslant 0$ for all k.

References

[1] E. Bansch, P. Morin, R.H. Nochetto, A finite-element method for surface diffusion: the parametric case, J. Comput. Phys. 203 (2005) 321–343.
[2] A.J. Bernoff, A.L. Bertozzi, T.P. Witelski, Axisymmetric surface diffusion: dynamics and stability of self-similar pinchoff, J. Statist. Phys. 93 (1998) 725–776.
[3] M. Burger, Numerical simulation of anisotropic surface diffusion with curvature-dependent energy, J. Comput. Phys. 203 (2005) 602–625.
[4] J.W. Cahn, Stability of rods with anisotropic surface free energy, Scripta Metall. 13 (1979) 1069–1071.
[5] J.W. Cahn, J.E. Taylor, Surface motion by surface diffusion, Acta Metall. Mater. 42 (1994) 1045–1063.
[6] B.D. Coleman, R.S. Falk, M. Moakher, Space-time finite-element methods for surface diffusion with applications to the theory of the stability of cylinders, SIAM J. Sci. Comput. 17 (1996) 1434–1448.
[7] B.D. Coleman, R.S. Falk, M. Moakher, Stability of cylindrical bodies in the theory of surface diffusion, Phys. D 89 (1995) 123–135.
[8] D.T. Danielson, D.K. Sparacin, J. Michel, L.C. Kimerling, Surface-energy-driven dewetting theory of silicon-on-insulator agglomeration, J. Appl. Phys. 100 (2006) 083507.
[9] K. Deckelnick, G. Dziuk, C.M. Elliott, Fully discrete finite element approximation for anisotropic surface diffusion of graphs, SIAM J. Numer. Anal. 43 (2005) 1112–1138.
[10] P. Du, Surface Energy Anisotropy Effects on the Stability of Nanowires, Louisiana Sate University, 2010.
[11] B. Fornberg, A Practical Guide to Pseudospectral Methods, Cambridge University Press, 1998.
[12] K.F. Gurski, G.B. McFadden, The effect of anisotropic surface energy on the Rayleigh instability, Proc. R. Soc. Lond. A 459 (2003) 2575–2598.
[13] K.F. Gurski, G.B. McFadden, M.J. Miksis, The effect of contact lines on the Rayleigh instability with anisotropic surface energy, SIAM J. Appl. Math. 66 (2006) 1163–1187.
[14] F. Hausser, A. Voigt, A discrete scheme for parametric anisotropic surface diffusion, J. Sci. Comput. 30 (2007) 223–235.
[15] E. Jiran, C.V. Thompson, Capillary instabilities in thin films, J. Elect. Mater. 19 (1990) 1153–1160.
[16] W. Kan, H. Wong, Fingering instability of a retracting solid film edge, J. Appl. Phys. 97 (2005) 043515.
[17] S. Karim, M.E. Toimil-Molares, A.G. Balogh, W. Ensinger, T.W. Cornelius, E.U. Khan, R. Neumann, Morphological evolution of Au nanowires controlled by Rayleigh instability, Nanotechnology 17 (2006) 5954–5959.
[18] C.M. Kennefick, R. Raj, Copper on sapphire: stability of thin films at 0.7 T_m, Acta Metall. 37 (1989) 2947–2952.
[19] M. Khenner, Motion of contact line of a crystal over the edge of solid mask in epitaxial lateral overgrowth, Comput. Mater. Sci. 32 (2005) 203–216.
[20] M. Khenner, R.J. Braun, M.G. Mauk, A model for isotropic crystal growth from vapor on a patterned substrate, J. Crystal Growth 235 (2002) 425–438.
[21] U.F. Mayer, Numerical solutions for the surface diffusion flow in three space dimensions, Comput. Appl. Math. 20 (2001) 361–379.
[22] M.S. McCallum, P.W. Voorhees, M.J. Miksis, S.H. Davis, H. Wong, Capillary instabilities in solid thin films: lines, J. Appl. Phys. 79 (1996) 7604–7611.
[23] D. Min, H. Wong, The effect of strong surface energy anisotropy on migrating grain-boundary grooves, J. Appl. Phys. 100 (2006) 053523.
[24] D. Min, H. Wong, Grain-boundary grooving by surface diffusion with asymmetric and strongly anisotropic surface energies, J. Appl. Phys. 99 (2006) 023515.
[25] D. Min, H. Wong, Rayleigh's instability of Lennard–Jones liquid nano-threads simulated by molecular dynamics, Phys. Fluids 18 (2006) 024103.
[26] T. Muller, K.-H. Heinig, B. Schmidt, Template-directed self-assembly of buried nanowires and the pearling instability, Mater. Sci. Eng. C 19 (2002) 209–213.
[27] W.W. Mullins, Flattening of a nearly plane solid surface due to capillarity, J. Appl. Phys. 30 (1959) 77–83.
[28] W.W. Mullins, Solid Surface Morphologies Governed by Capillarity, Metal Surfaces, Am. Soc. Metals, Metals Park, Ohio, 1963. pp. 17–66.
[29] W.W. Mullins, Theory of thermal grooving, J. Appl. Phys. 28 (1957) 333–339.
[30] F.A. Nichols, W.W. Mullins, Surface-(Interface-) and volume-diffusion contributions to morphological changes driven by capillarity, Trans. Metall. Soc. AIME 233 (1965) 1840–1848.
[31] J.A.F. Plateau, Experimental and theoretical researches on the figures of equilibrium of a liquid mass withdrawn from the action of gravity, Annual Report of the Board of Regents and Smithsonian Institution (1863) 207–285;
J.A.F. Plateau, Experimental and theoretical researches on the figures of equilibrium of a liquid mass withdrawn from the action of gravity, Annual Report of the Board of Regents and Smithsonian Institution (1864) 286–369;
J.A.F. Plateau, Experimental and theoretical researches on the figures of equilibrium of a liquid mass withdrawn from the action of gravity, Annual Report of the Board of Regents and Smithsonian Institution (1865) 411–435;
J.A.F. Plateau, Experimental and theoretical researches on the figures of equilibrium of a liquid mass withdrawn from the action of gravity, Annual

Report of the Board of Regents and Smithsonian Institution (1866) 255–289;
J.A.F. Plateau, Experimental and theoretical researches on the figures of equilibrium of a liquid mass withdrawn from the action of gravity, Annual Report of the Board of Regents and Smithsonian Institution (1863) 207–285.
[32] L. Rayleigh, On the instability of jets, Proc. London Math. Soc. 10 (1879) 4–13.
[33] P. Smereka, Semi-implicit level set methods for curvature and surface diffusion motion, J. Sci. Comput. 19 (2003) 439–455.
[34] K.A. Smith, F.J. Solis, D.L. Chopp, A projection method for motion of triple junctions by level sets, Interfaces Free Bound. 4 (2002) 263–276.
[35] D.J. Srolovitz, S.A. Safran, Capillary instabilities in thin films. I. Energetics, J. Appl. Phys. 60 (1986) 247–254.
[36] D.J. Srolovitz, S.A. Safran, Capillary instabilities in thin films. II. kinetics, J. Appl. Phys. 60 (1986) 255–260.
[37] M.E.T. Toimil-Molares, A.G. Balogh, T.W. Cornelius, R. Neumann, C. Trautmann, Fragmentation of nanowires driven by Rayleigh instability, Appl. Phys. Lett. 85 (2004) 5337–5339.
[38] G. Tryggvason, B. Bunner, A. Esmaeeli, D. Juric, N. Al-Rawahi, W. Tauber, J. Han, S. Nas, Y.-J. Jan, A front-tracking method for the computations of multiphase flow, J. Comput. Phys. 169 (2001) 708–759.
[39] C.E. Weatherburn, Differential invariants in geometry of surfaces, with applications to mathematical physics, Quart. J. Math. 50 (1925) 230.
[40] H. Wong, Unpublished (2009).
[41] H. Wong, M.J. Miksis, P.W. Voorhees, S.H. Davis, Universal pinch off of rods by capillarity-driven surface diffusion, Scripta Mater. 39 (1998) 55–60.
[42] H. Wong, P.W. Voorhees, M.J. Miksis, S.H. Davis, Periodic mass shedding of a retracting solid film step, Acta Mater. 48 (2000) 1719–1728.
[43] F. Yin, R.E. Palmer, Q. Guo, Faceting of nanoscale fingers on the (1 1 1) surface of gold, Surf. Sci. 600 (2006) 1504–1509.
[44] W. Zhang, Evolution of crystal morphologies to equilibrium by surface diffusion with anisotropic surface free energy in three dimensions, J. Crystal Growth 297 (2006) 169–179.
[45] K. Zhao, R.S. Averback, D.G. Cahill, Patterning of metal nanowires by directed ion-induced dewetting, Appl. Phys. Lett. 89 (2006).